Pergamon

J. Biomechanics, Vol. 28, No. 8, pp. 901–914, 1995

0021-9290/95 $9.50 + .00

0021-9290(94)00157-X

A THEORETICAL MODEL OF CIRCULATORY INTERSTITIAL FLUID FLOW AND SPECIES TRANSPORT WITHIN POROUS CORTICAL BONE

Russell G. Keanini,*† Robert D. Roer‡ and Richard M. Dillaman‡

*Department of Mechanical Engineering and Engineering Science, University of North Carolina at Charlotte, Charlotte, NC 28223, U.S.A.; ‡Center for Marine Science Research and Department of Biological Sciences, University of North Carolina at Wilmington, Wilmington, NC 28403, U.S.A.

Abstract—A three-dimensional model of interstitial fluid flow and passive species transport within mineralized regions surrounding cross-cortical vessel canals is developed. In contrast to earlier studies, the present model applies to circulatory, non-stress-induced interstitial flow in porous cortical bone. Based on previous experimental observations, the canals are modeled as line sources that pass at an oblique angle through the cortex. Cross-cortical interstitial flow from the endosteal surface to the periosteal surface is also taken into account. It is found that model transport characteristics are qualitatively consistent with reported observations. In addition, parametric studies reveal the following: (1) Solute contact with the matrix is maximized when the ratio of canal radius to cortex thickness (R) is near physiological R values. (2) Solute-matrix contact falls to low levels when R falls below the physiological range. (3) Solute-matrix contact is maximized when the cross-cortical velocity is approximately an order of magnitude smaller than the canal outflow velocity. The first and second findings suggest that within porous bone physiological ranges of R promote near optimal species contact with the mineralized matrix. The third finding suggests that relatively impermeable layers of bone within the cortex can effectively promote solute-matrix contact by limiting cross-cortical flow. Finally, the model suggests that intra-canal resorption associated with reduced external loading may effectively compensate for reduced stress-induced interstitial flow by enhancing circulatory interstitial flow and species transport.

Keywords: Bone; Flow; Model.

NOMENCLATURE

ϕ_0	canals' angle of inclination relative to the bone's long axis
$R^*;R$	dimensional and dimensionless canal radius $[R = R^*/T^*]$
T^*	dimensional cortex thickness
$\overline{P^*};P$	dimensional and dimensionless time-averaged fluid pressure $[P = (\overline{P^*} - \overline{P_e^*})/\overline{\Delta P^*}]$
$\overline{u^*},\overline{v^*},\overline{w^*}$	dimensional time-averaged x-, y-, and z-velocity components
u,v,w	dimensionless time-averaged x-, y-, and z-velocity components $[(u,v,w) = (\overline{u^*},\overline{v^*},\overline{w^*})/\overline{\Gamma^*}]$
$m^*;m$	dimensional and dimensionless source strength $[m^* = \overline{V^*}R^*; m = \overline{V^*}R^*/(\overline{\Gamma^*}T^*)]$
k	permeability
$t^*;t$	dimensional and dimensionless time $[t = t^*/(T^*/\overline{\Gamma^*})]$
t_0^*	period for one cardiac cycle
$\overline{V^*}$	dimensional time-averaged outward radial velocity at the canal wall
$\overline{\Gamma^*}$	characteristic cross-cortical velocity component $[\overline{\Gamma^*} = k(\overline{P_e^*} - \overline{P_p^*})/(T^*\mu)]$
$\overline{P_e^*}$	dimensional time-averaged endosteal pressure
$\overline{P_p^*}$	dimensional time-averaged periosteal pressure
μ	fluid viscosity
$\overline{\Delta P^*}$	dimensional time-averaged pressure difference across the cortex $[\overline{\Delta P^*} = \overline{P_e^*} - \overline{P_p^*}]$
Ω	solution domain
Ω_e	subvolume within solution domain
P_{cc}	dimensionless time-averaged cross-cortical pressure contribution
P_{ls}	dimensionless time-averaged pressure produced by several line sources
N	total number of sources used to calculate P_{ls}
$\mathbf{r}_J(t;\theta_i,z_k)$	instantaneous dimensionless position vector of solute particle which originated from source J at angular position θ_i and longitudinal position z_k
$V^*;V$	dimensional and non-dimensional radial fluid velocity at the canal wall $[V = V^*\mu R^*/(k\overline{\Delta P^*})]$
$\overline{\Gamma_0^*}$	dimensional-time averaged cross-cortical velocity component
Γ_0	dimensionless time-averaged cross-cortical velocity component $[\Gamma_0 = \overline{\Gamma_0}^*/\overline{\Gamma^*}]$
Δt	dimensionless time increment $[\Delta t = \Delta t^*/(T^*/\overline{\Gamma^*})]$
ϕ_i	linear weight function
$L^*;L$	dimensional and dimensionless canal length $[L = L^*/T^*]$
x^*,y^*,z^*	dimensional Cartesian coordinates
x,y,z	dimensionless Cartesian coordinates $[(x,y,z) = (x^*,y^*,z^*)/T^*]$
$\nabla^*;\nabla$	dimensional and dimensionless gradient operators (defined following equations (4) and (5))

Superscripts and diacritical marks

*	dimensional quantity
–	time-averaged quantity; distance (Appendix A)

Received in final form 30 *October* 1994.
†Author for correspondence.

INTRODUCTION

Current theoretical understanding of fluid flow and species transport within cortical bone remains limited and specialized. Almost all prior work in this area has focused on flow and transport within osteons (Johnson *et al.*, 1982; Kufahl and Saha, 1990; McCarthy and Yang, 1992; Petrov *et al.*, 1989; Piekarski and Munro, 1977; Pollack *et al.*, 1984; Willans and McCarthy, 1986). In contrast, theoretical study of interstitial flow and species transport within porous cortical bone has not been undertaken. (Following Montgomery *et al.* (1988), we define *interstitial flow* as flow that occurs within both canaliculi *and* pores within the matrix. In addition, based on the finding that ferritin (diameter ~ 10 nm) often moves rapidly through the extra-canalicular porous region (Dillaman, 1984; Montgomery *et al.*, 1988), we define *porous cortical bone* as bone in which the average extra-canalicular pore size is approximately 10 nm or greater.) Since juvenile bone and significant portions of adult bone in various species fall within this classification, then theoretical flow modeling should provide insight into potential flow and nutrient transport pathways within this important bone type.

Circulatory cortical flow, i.e. interstitial flow driven by the heart, may play an important role in cortical species transport (Dillaman *et al.*, 1991), particularly within developing and non-weight bearing bone. Indeed, circulatory flow has been shown capable of sustaining non-stress-induced cross-cortical streaming potentials within canine tibias (Otter *et al.*, 1990). However, as in the case of porous cortical interstitial flow, it appears that circulatory cortical flow has not received theoretical attention.

Strong experimental evidence indicates that significant circulatory interstitial flow occurs within porous cortical bone (Doty *et al.*, 1976; Dillaman, 1984; Montgomery *et al.*, 1988; Roer *et al.*, 1988). For example, Dillaman (1984), studying flow in non-stressed chick femurs, found that intravascularly injected ferritin appeared within the mineralized region within 5 min of injection. In horizontal cross-section, the ferritin typically formed discrete, semi-elliptical bands around each vessel canal (Fig. 1(a)–(c)), while longitudinal cross-sections revealed that the bands often remained nearly parallel to the canals' long axes (Fig. 1(d)). Montgomery *et al.* (1988) reported similar findings within adult canine tibias. A number of studies have also reported evidence of *centrifugal* circulatory interstitial flow, wherein fluid moves interstitially from the endosteal to the periosteal surface (Brooks, 1970; Dillaman, 1984; Montgomery *et al.*, 1988; Otter *et al.*, 1990; Seliger, 1971). It is generally believed that this centrifugal, or as we will term it, cross-cortical flow, is driven by fluid pressure gradients across the cortex (Brooks, 1970; Dillaman, 1984; McCarthy and Yang, 1992; Otter *et al.*, 1990). Importantly, both near-canal and cross-cortical interstitial transport appear to reflect bulk interstitial fluid flow rather than diffusion since solute markers remain well defined as they propagate through the matrix (Dillaman, 1984; McCarthy and Yang, 1992; Montgomery *et al.*, 1988). Circulatory interstitial flow is clearly evidenced since apparent bulk interstitial transport has been observed in anesthetized test subjects (Dillaman, 1984; Montgomery *et al.*, 1988).

The objective of this paper is to develop a simple model of circulatory, non-stress-induced interstitial flow and species transport within porous cortical bone, focusing in particular on flow and transport within mineralized regions surrounding cross-cortical vessel canals. Model flow and transport predictions are compared against the experimental observations reported by Dillaman (1984) and Montgomery *et al.* (1988). In addition, using non-dimensional parameters representative of a wide range of possible conditions, the model is used to investigate the effects of canal radius, canal orientation, and cross-cortical interstitial flow on overall flow and species transport characteristics.

METHODS

In order to compare model predictions against experimental results, we will arrange vessel canals in a manner similar to those observed in two-day-old chick femurs (Fig. 1). In addition, in order to minimize computational requirements, we will limit our attention to a region, Ω, containing ten vessel canals (Fig. 2). It is important to note that the arrangement and number of canals can be readily modified. The model itself is based on the following assumptions.

(1) The vessel canals are mutually parallel and pass obliquely from the endosteal to the periosteal surface of the cortex.

(2) The vessels' long axes form an angle ϕ_0 with the endosteal surface (Fig. 2(c)).

(3) Every canal is circular and has a radius R^*.

(4) The azimuthal angle (about the bone's long axis) which encompasses the solution domain is small enough that the azimuthal cross-section can be taken as rectangular (Figs 1(c) and 2(a)).

(5) In order to simulate the effect of flow induced by vessel canals lying outside the solution domain, Ω, we assume that the arrangement of vessel canals (Fig. 2(b)) repeats itself in the azimuthal direction.

(6) The matrix is a homogeneous continuous medium (Petrov *et al.*, 1989).

(7) Permeability is homogeneous and isotropic, and thus constant.

(8) Flow within the porous matrix is incompressible and governed by Darcy's law (see equation (4) below).

(9) In order to simulate circulatory pressure and velocity variations, we assume that pressure and velocity are composed of a steady, time-averaged component plus a perfectly cyclic, time-dependent com-

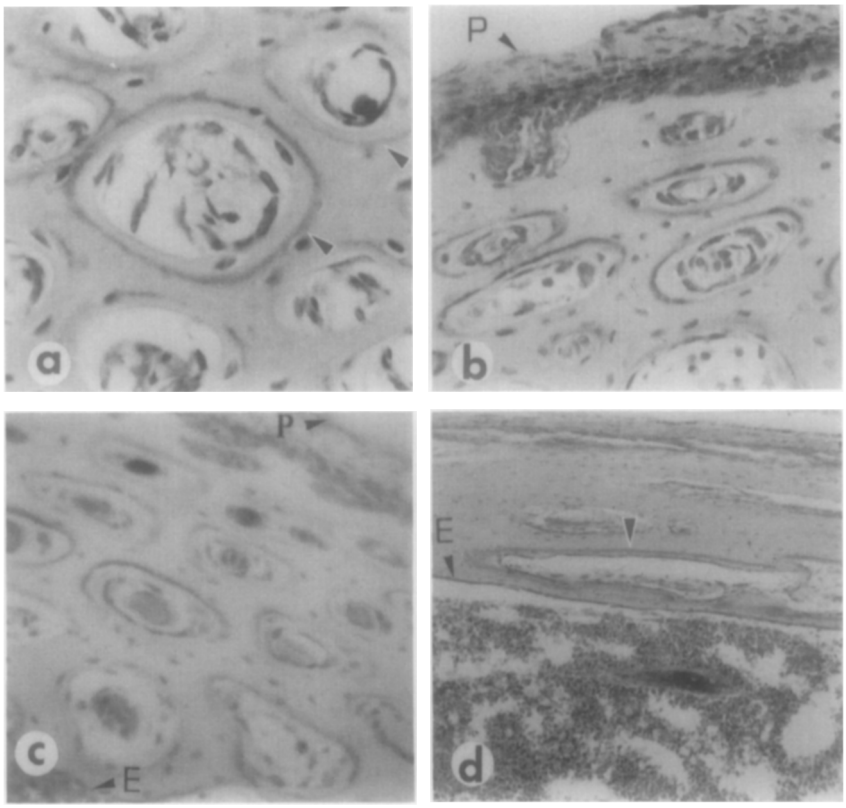

Fig. 1. Micrographs showing position of ferritin within chick cortical bone in the vicinity of cross-cortical vessel canals (from Dillaman, 1984). Ferritin was injected for 2 min (at 0.1 ml min^{-1}) into the jugular vein and the specimen were gathered 5 mins after injections ceased. (a)–(c) Lateral cross-sections show bands of ferritin around all canals (typical bands shown by arrows). Note that osteocytic lacunae appear as small, dye-filled semi-ellipsoids around each canal. (d) Longitudinal cross-section shows a ferritin band (arrow) essentially parallel to the parent vessel canal. Magnifications are: a, 1000×; b and c, 750×; d, 575×. The periosteal surface, denoted by *P*, is visible near the top of (b) and (c) and is located above the top edge of (a) and (d). The endosteal surface, denoted by *E*, is located at the lower left corner of (c), near the center of (d), and immediately below the bottom edges of (a) and (b).

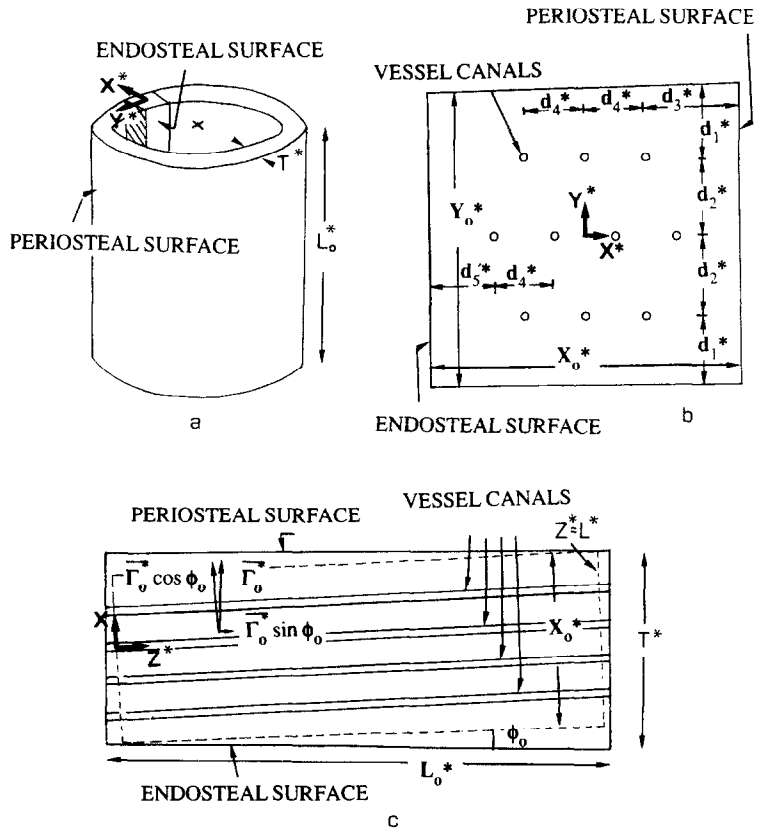

Fig. 2. Model geometry. (a) Modeled region shown relative to bone shaft. Note, x- and y-axes tilt at an angle ϕ_0 relative to the shaft's long axis. (b) Top view of modeled region. (c) Lateral view of modeled region (located within the dotted lines). The view in (c) corresponds to the cross-hatched region in (a). The cross-cortical velocity component $\overline{\Gamma_0^*}$ is shown in (c) along with its components in the x^*- and z^*-directions. In all calculations, $T^* = 250\ \mu m$, $X_0^* = 200\ \mu m$, $Y_0^* = 185.2\ \mu m$, $d_1^* = 55.6\ \mu m$, $d_2^* = 37.0\ \mu m$, $d_3^* = 70.4\ \mu m$, $d_4^* = 29.6\ \mu m$, and $d_5^* = 55.6\ \mu m$. The length L^* of the solution domain is given by $L^* = (L_0^* - T^* \tan\phi_0)\cos\phi_0$, where $L_0^* = T^*(1 + \sin^2\phi_0)/(\sin\phi_0 \cos\phi_0) - X_0^*/\sin\phi_0$. (Note, the last two relationships are derived in Appendix A.)

ponent:

$$(P^*,u^*,v^*,w^*) = (\overline{P^*},\overline{u^*},\overline{v^*},\overline{w^*}) + (P',u',v',w'), \quad (1)$$

where averaging is performed over one cardiac cycle, t_0^*:

$$(\overline{P^*},\overline{u^*},v^*,\overline{w^*}) = \frac{1}{t_0^*}\int_{t*}^{t*+t_0^*} (P^*,u^*,v^*,w^*)\,dt^* \quad (2)$$

and where time-dependent components are denoted with a prime. Throughout this paper, x-, y-, and z-velocity components are denoted by u, v, and w, respectively, while pressure is denoted by P. Dimensional quantities are denoted with asterisks while non-dimensional quantities are not starred. Notice that $\overline{P'},\overline{u'},\overline{v'}$, and $\overline{w'}$ are all equal to zero and that steady and time-dependent components are, in general, spatially dependent.

(10) Time-averaged pressures on the endosteal and periosteal surfaces are constant. However, in accord with evidence that a pressure gradient exists across the cortex (Brooks, 1971; Dillaman, 1984; Otter *et al.*, 1990), average pressures on each surface assume different magnitudes.

(11) A cross-cortical interstitial flow, denoted by the velocity vector $\overline{\Gamma_0^*}$ in Fig. 2(c), and driven by the time-averaged cross-cortical pressure gradient, is assumed to exist.

(12) Consistent with the fact that solute markers typically form semi-elliptical bands or haloes around vessel canals (Dillaman, 1984; Montgomery, 1988), we model outflow from each vessel canal as line source flow. In addition, all line sources have the same strength, m^*, where m^* is defined as $m^* = \overline{V^*}R^*$ and where $\overline{V^*}$ is the time-averaged radial outflow velocity at the canal wall. (Consider a cylindrical coordinate system. In *line source flow*, fluid flows radially outward from a line that is parallel to the z-axis. At any given radial distance r^* from the line, velocities are purely radial and are given by $\mathbf{u}^* = (m^*/r^*)\,\hat{\mathbf{e}}_r$, where again m^* is the dimensional source strength. See, e.g. Fox and McDonald, 1992.)

(13) Finally, in accord with the observation that ferritin rings within the matrix remain well defined as they propagate through the matrix (Dillaman, 1984; Montgomery *et al.*, 1988), we neglect solute dispersion and diffusion. The validity of most of these assumptions is considered in the Discussion section below.

In order to efficiently consider a wide range of conditions, it proves convenient to cast the problem in terms of non-dimensional variables. Here non-dimensionalization is carried out as follows:

$$(x,y,z) = (x^*/T^*, y^*/T^*, z^*/T^*)\ (u,v,w)$$
$$= (\overline{u^*}/\overline{\Gamma^*}, \overline{v^*}/\overline{\Gamma^*}, \overline{w^*}/\overline{\Gamma^*}),$$
$$P = \overline{P^*}/\overline{\Delta P^*}, \tag{3}$$

where T^* is the thickness of the cortex, $\overline{\Gamma^*} = k(\overline{P_e^*} - \overline{P_p^*})/(T^*\mu)$ is the characterisitic time-averaged cross-cortical velocity, and u,v,w and $\overline{u^*},\overline{v^*},\overline{w^*}$ are the time-averaged dimensionless and dimensional x-, y-, and z-velocity components. In addition, $\overline{\Delta P^*} = \overline{P_e^*} - \overline{P_p^*}$, is the time-averaged pressure difference across the cortex, and $\overline{P_e^*}$ and $\overline{P_p^*}$ are the time-averaged pressures on the endosteal and periosteal surfaces. The overbar has been dropped from non-dimensional variables for convenience. Characteristic dimensional parameter values, obtained from various species, are given in Table1. Based on the definitions above, the dimensionless source strength, m, is given by $m = \overline{V^*}R^*/(\overline{\Gamma^*}T^*)$. Due to potential variations in permeability near the periosteal (Montgomery *et al.*, 1988) and/or endosteal surfaces (Dillaman *et al.*, 1991), we will allow for the possibility that the *actual* cross-cortical velocity ($\overline{\Gamma_0^*}$) within Ω is not necessarily equal to the arbitrarily defined cross-cortical velocity scale, $\overline{\Gamma^*}$. We will, however, assume that the time-averaged cross-cortical pressure difference ($\overline{\Delta P^*}$) and cross-cortical velocity component ($\overline{\Gamma_0^*}$) are constant within Ω. The non-dimensional cross-cortical velocity component will be defined as $\Gamma_0 = \overline{\Gamma_0^*}/\overline{\Gamma^*}$.

The time-averaged form of Darcy's law is given by

$$\overline{\mathbf{u}^*} = \frac{-k}{\mu}\nabla^*\overline{P^*}, \tag{4}$$

where equations (1) and (2) have been used and where k is the permeability, μ is the fluid viscosity, and $\nabla^* = (\partial/\partial x^*)\,\hat{\mathbf{e}}_x + (\partial/\partial y^*)\,\hat{\mathbf{e}}_y + (\partial/\partial z^*)\,\hat{\mathbf{e}}_z$ is the gradient operator. Note that the instantaneous form of equation (4) is obtained by simply replacing averaged quantities with their instantaneous counterparts. Since external loading is not considered, time-varying porosity changes can be neglected (Johnson *et al.*, 1982) so that the time-averaged continuity equation assumes the form

$$\nabla^* \cdot \overline{\mathbf{u}^*} = 0. \tag{5}$$

Using the non-dimensional variables defined in equation (3) and defining $\nabla = (\partial/\partial x)\,\hat{\mathbf{e}}_x + (\partial/\partial y)\,\hat{\mathbf{e}}_y + (\partial/\partial z)\,\hat{\mathbf{e}}_z$, we obtain the dimensionless time-averaged form of Darcy's law

$$\mathbf{u} = \nabla P \tag{6}$$

and the corresponding dimensionless continuity equation

$$\nabla \cdot \mathbf{u} = 0. \tag{7}$$

Finally, replacing $\mathbf{u}$ in equation (7) with the right-hand side of equation (6), we obtain the governing equation for the dimensionless, time-averaged interstitial fluid pressure field

$$\nabla^2 P = 0. \tag{8}$$

Based on the assumptions listed above and noting that line sources are fundamental solutions of equation (8), the time-averaged pressure field within Ω is obtained by superposing the time-averaged cross-cortical pressure contribution with the time-averaged pressure induced by all of the canals (line sources) interior and exterior to Ω. Considering first the cross-cortical pressure contribution, P_{cc}, the dimensionless cross-cortical velocity, Γ_0, can be resolved into a com-

Table 1. Approximate dimensional parameter values

Parameter	Symbol	Approximate magnitude	Species
Cortex thickness	T^*	2.5 (10^{-5}) m	Chicken*
Cortex thickness	T^*	9.0 (10^{-3}) m	Human†
Vessel canal radius	R^*	2.7 (10^{-6}) m	Chicken
Vessel canal radius	R^*	5 (10^{-5}) m	Human‡
Canal angle	ϕ_0	$10^\circ \leqslant \phi_0 \leqslant 20^\circ$	Chicken
Cross-cortical pressure difference	$\overline{\Delta P^*}$	5330 N m^{-2}	Dog§
Permeability	k	10^{-14} m$^2 \leqslant k \leqslant 10^{-11}$ m^2	Rat¶
Fluid viscocity	μ	2 (10^{-3}) kg m^{-1} s^{-1}	Note 5

*Data for chicken taken from Dillaman (1984).
†Mihalko *et al.* (1992).
‡Pollack *et al.* (1984).
§Otter *et al.* (1990).
¶Dillaman *et al.* (1991).

ponent, $\Gamma_0 \sin\phi_0$, parallel to the z-axis and a component, $\Gamma_0 \cos\phi_0$, parallel to the x-axis (Fig. 2(c)). Thus, from equation (6), the pressure component (P_{cc}) which drives the cross-cortical flow is given by

$$P_{cc} = \Gamma_0 \cos\phi_0 x + \Gamma_0 \sin\phi_0 z. \quad (9)$$

From this equation it is clear that a constant cross-cortical velocity component, Γ_0, corresponds to a linearly varying pressure contribution, P_{cc}, across the cortex. Dillaman's (1984) heuristic model of pressure driven flow within the cortex implicitly assumed the same linear cross-cortical pressure variation. Thus, the present model is fully consistent with Dillaman's (1984) earlier model while extending that work by providing a quantitative interpretation for radial outflow from the canals (see next paragraph).

Considering next the pressure induced by outflow from cross-cortical canals, P_{ls}, we note that the pressure, P_j, induced at a point (x,y,z) by a single line source passing through the point (x_j,y_j) (parallel to the z-axis) is given by

$$P_j = m \ln[(x - x_j)^2 + (y - y_j)^2]^{1/2}, \quad (10)$$

where m is the dimensionless source strength. Thus, the interstitial pressure induced by N canals, located both within and outside the solution domain, is obtained by summing all of the individual pressure contributions. The result is given by

$$P_{ls} = m \sum_{j=1}^{N} \ln[(x - x_j)^2 + (y - y_j)^2]^{1/2}, \quad (11)$$

where we have assumed that each of the N sources are of strength m. Since the time-averaged three-dimensional interstitial pressure field within the solution domain is the sum of P_{cc} and P_{ls}, the three-dimensional interstitial flow field, obtained from equation (6), is given by

$$\mathbf{u} = \nabla P = \nabla\left[m \sum_{j=1}^{N} \ln[(x - x_j)^2 + (y - y_j)^2]^{1/2} + \Gamma_0(x \cos\phi_0 + z \sin\phi_0)\right]. \quad (12)$$

Since species diffusion and dispersion are neglected, species transport is driven strictly by the interstitial flow field. Thus, a particle tracking scheme can be employed in order to determine the temporal movement of solute within the interstitial space. A system of seven repeating arrays of 10 canals each are arranged in the y-direction. (A unit array is shown in Figs 2 (b) and 2(c).) These are used to generate the time-averaged pressure component P_{ls} within the solution domain (corresponding to the central, or fourth unit array). (Results remain essentially unchanged when more than seven arrays are used in the calculation.) In order to simulate solute transport following injection of a small amount of solute (Dillaman, 1984; Montgomery *et al.*, 1988), it is assumed that all solute particles leave the canals at time zero. Let $\mathbf{r}_J(t;\theta_i,z_k)$ denote the time-varying position of the solute particle which originated from source J at angular position θ_i and longitudinal position z_k. At each of 10 longitudinal positions, z_k (where $z_1 = 0$, $z_2 = L/9, \ldots, z_{10} = L$), solute particles are initially placed at 32 equiangular positions (θ_i) around the circumference of each canal ($\theta_1 = \pi/16$, $\theta_2 = \pi/8, \ldots$, $\theta_{32} = 2\pi$). Thus, 320 particles are initially placed at the wall of each of the 10($= J$) canals. Since diffusion does not occur, updates of $\mathbf{r}_J(t;\theta_i,z_k)$ are carried out using

$$\mathbf{r}_J(t + \Delta t;\theta_i,z_k) = \mathbf{r}_J(t;\theta_i,z_k) + \mathbf{u}(\mathbf{r}_J(t;\theta_i,z_k))\,\Delta t, \quad (13)$$

where $\mathbf{u}(\mathbf{r}_J(t;\theta_i,z_k))$ is the time-averaged velocity at position $\mathbf{r}_J(t;\theta_i,z_k)$, and where $\Delta t(= \Delta t^*/T^*/\overline{\Gamma^*})$ is the dimensionless time step.

The solution domain is subdivided into 72 equal increments in both the x- and y-directions and into 200 increments in the z-direction; equivalently, the domain is discretized using $73 \times 73 \times 201$ nodes. The dimensional length L^* of the solution domain is given by $L^* = (L_0^* - T^* \tan\phi_0)\ \cos\phi_0$, where $L_0^* = T^*(1 + \sin^2\phi_0)/(\sin\phi_0 \cos\phi_0) - X_0^*/\sin\phi_0$ and where X_0^* is the length of Ω in the x-direction (refer to Fig. 2 and to Appendix A). Based on Dillaman's (1984) morphological data (reproduced, in part, in Fig.1), all calculations assume $X_0^* = 200\ \mu$m, $Y_0^* = 185\ \mu$m and $T^* = 250\ \mu$m, where Y_0^* is the azimuthal length of the solution domain. The distances d_1^*–d_5^* (Fig. 2(b)) are similarly based on Dillaman (1984).

Velocities at each node are generated using equation (12). Given the particle position $\mathbf{r}_J(t;\theta_i,z_k)$, which lies within some brick shaped subvolume, Ω_e, of the solution domain, the velocity $\mathbf{u}(\mathbf{r}_J(t;\theta_i,z_k))$ in equation (13) is determined by linearly interpolating the subvolume's eight nodal velocities $\mathbf{u}_i$:

$$\mathbf{u}(x,y,z) = \sum_{i=1}^{8} \phi_i \mathbf{u}_i, \quad (14)$$

where $\mathbf{u}_i$ is the velocity at the ith vertex of Ω_e (calculated from equation (12)) and ϕ_i is the corresponding linear weighting function (see, e.g. Zienkiewicz, 1977). This approach proves much more efficient than calculating the non-nodal velocities $\mathbf{u}(\mathbf{r}_J(t;\theta_i,z_k))$ from equation (12). The species transport calculation is stopped when all 3200 particles pass out of the solution domain. The fraction of bone contacted by solute within the solution domain is determined by summing all of the subvolumes contacted by the particles. This is a fairly accurate approximation since the maximum ratio of subvolume volume to total volume is of the order of 10^{-6}. It was found that convergent values for the fraction of bone contacted could be obtained for time steps (Δt) smaller than 5; $\Delta t = 2$ in all solute contact calculations presented below. (For clarity, $\Delta t = 20$ when succeeding solute front positions are plotted. In addition, the fraction of bone contacted by solute is expressed as a percentage in Figs 5 and 7, as discussed below.)

The non-dimensional parameter ranges that we examine are listed in Table 2. It is important to note

Table 2 Non-dimensional parameter ranges

Parameter	Range
Canal radius (R)	$10^{-5} \leqslant R \leqslant 10^{-1}$
Cross-cortical velocity (Γ_0)	$0 \leqslant \Gamma_0 \leqslant 1$
Source strength (m)	$0 \leqslant m \leqslant 10^{-1}$
Canals' angle of inclination (ϕ_0)	$10^\circ \leqslant \phi_0 \leqslant 20^\circ$

that a complete set of values for $T^*, R^*, k, \overline{\Delta P^*}, \overline{V^*}$, and Γ^*, taken from a single species, does not appear to exist. Thus, it is appropriate to examine flow and transport characteristics over physically relevant parameter *ranges* rather than at a single ill-defined set of parameter values. In order to identify appropriate ranges for Γ_0 and m, we first identify the appropriate velocity scale, i.e., the approximate maximum velocity in the problem. In the case of flow within chick femurs, it is straightforward to show that the velocity scale is set by the characteristic cross-cortical velocity, $\overline{\Gamma^*}$. In particular, a conservative estimate of $\overline{\Gamma^*}$, obtained using $\overline{\Delta P^*} \sim 5330\,\mathrm{N\,m^{-2}}$, $\mu \sim 0.002\,\mathrm{kg\,m^{-1}\,s^{-1}}$, $T^* \sim 2.5(10^{-4})\,\mathrm{m}$, and a relatively small permeability of $k \sim 10^{-14}\,\mathrm{m^2}$ (refer to Table 1), indicates that $\overline{\Gamma^*}$ is, at minimum, on the order of $\sim 10^{-4}\,\mathrm{m\,s^{-1}}$. On the other hand, the outflow velocity, $\overline{V^*}$, estimated by dividing the average ferritin displacement (Fig. 1) by the known 7 min time interval, is approximately equal to $6(10^{-8})\,\mathrm{m\,s^{-1}}$. Thus, since a conservative estimate of $\overline{\Gamma^*}$ is approximately three orders of magnitude larger than $\overline{V^*}$, then $\overline{\Gamma^*}$ clearly determines the velocity scale. Due to permeability variations near the endosteal and/or periosteal surfaces, the actual cross-cortical velocity ($\overline{\Gamma_0^*}$) can assume values between zero and $\overline{\Gamma^*}$. Thus, the appropriate range of values for the dimensionless cross-cortical velocity ($\Gamma_0 = \overline{\Gamma_0^*}/\overline{\Gamma^*}$) is $0 \leqslant \Gamma_0 \leqslant 1$. Notice that this is the appropriate range for Γ_0 regardless of the actual value of $\overline{\Gamma^*}$. With regard to the appropriate range for the non-dimensional source strength m, we note that m is equal to the non-dimensional velocity at the canal wall ($V = \overline{V^*}/\overline{\Gamma^*}$) multiplied by the non-dimensional canal radius R. Since the largest realistic value of R is of the order of 0.1 (Jowsey and Gordan, 1971) and since the maximum value of V is 1 (i.e. the maximum possible value of $\overline{V^*}$ is $\overline{\Gamma^*}$), then the appropriate range for m is $0 \leqslant m \leqslant 0.1$. Note that the range of R we examine (Table 2) is expected to encompass all physiologically relevant R values and that the range for ϕ_0 is based on Dillaman's (1984) observations in chick femurs.

Prior to carrying out parametric studies, we define a *reference* flow field that roughly corresponds to flow in chick femurs (Dillaman, 1984). Reference values for R and m are obtained using $R^* = 2.5(10^{-6})$ m, $T^* = 2.5(10^{-4})\ \mathrm{m\,s^{-1}}$, and $\overline{V^*} = 6(10^{-8})\ \mathrm{m\,s^{-1}}$ (all based on Dillaman, 1984) and by arbitrarily setting $\overline{\Gamma^*} = 10^{-4}\,\mathrm{m\,s^{-1}}$ (see last paragraph). Thus, in the reference flow, $R = R^*/T^* = 0.01$, and $m = 6(10^{-6})$. It is important to realize that we are free to set the value of $\overline{\Gamma^*}$ since $\overline{\Gamma^*}$ merely serves as a scale factor for all velocities in the problem. Since the canals' angle of inclination over most of the chick's femoral shaft is approximately 10° (Dillaman, 1984), we choose this as the reference value for ϕ_0. Unfortunately, the cross-cortical velocity ($\overline{\Gamma_0^*}$) in Dillaman's (1984) study is unknown. In an attempt to obtain a rough estimate of $\overline{\Gamma_0^*}$, or equivalently, Γ_0, trial and error simulations were run until predicted flow characteristics were qualitatively similar to those observed by Dillaman (1984). Since a family of such flows was found over the range $0 \leqslant \Gamma_0 \leqslant 10^{-5}$, we arbitrarily set the reference value of Γ_0 equal to $m(\Gamma_0 = m = 6(10^{-6}))$. In order to account for the fact that experimental cross-sections cut across the canal array at an angle (Fig. 2), plotted solute positions (Figs 5 and 7) are images that are resolved from the plane $z = 1$ onto the plane of cross-section.

RESULTS

Qualitative solute transport characteristics for the reference flow show that at early times following solute release, semi-elliptical haloes form around each canal (Fig. 3). At later times, the elliptical haloes deform and stretch as they propagate around other vessel canals within the solution domain (Fig. 3(b)). A slight asymmetry in the pattern of solute movement is detectable where solute fronts are displaced slightly toward the periosteal surface.

The volume of matrix contacted by the solute (which we will refer to as solute coverage) increases with increasing canal radius (Figs 4 and 5). The increase from low to high levels of solute coverage essentially occurs over a single decade in R (i.e. $0.001 \leqslant R \leqslant 0.01$) while coverage is essentially complete for $R > \sim 0.01$. Over the range $10^{-5} \leqslant R \leqslant 10^{-3}$, coverage slowly increases from approximately 7 to 25%. Under the range of conditions investigated, solute coverage is essentially independent of the angle of inclination ϕ_0 (Fig. 4).

At cross-cortical velocities (Γ_0) less than approximately 0.0001, and for any of the given canal radii (R), solute coverage varies little with decreasing Γ_0 (Fig. 6). In contrast, solute coverage decreases with increasing cross-cortical velocity when $\Gamma_0 > \sim 0.0001$. For each given R, solute coverage is greatest when Γ_0 is less than approximately 0.0001 and approaches zero for Γ_0 greater than ~ 0.01. Coverage at each value of R is again nearly independent of the angle of inclination (Fig. 6). Qualitatively, when the cross-cortical velocity is zero, solute coverage is at all times symmetric with respect to both vertical and horizontal center lines within the solution domain (Fig. 7(a)). However, coverage becomes increasingly asymmetric,

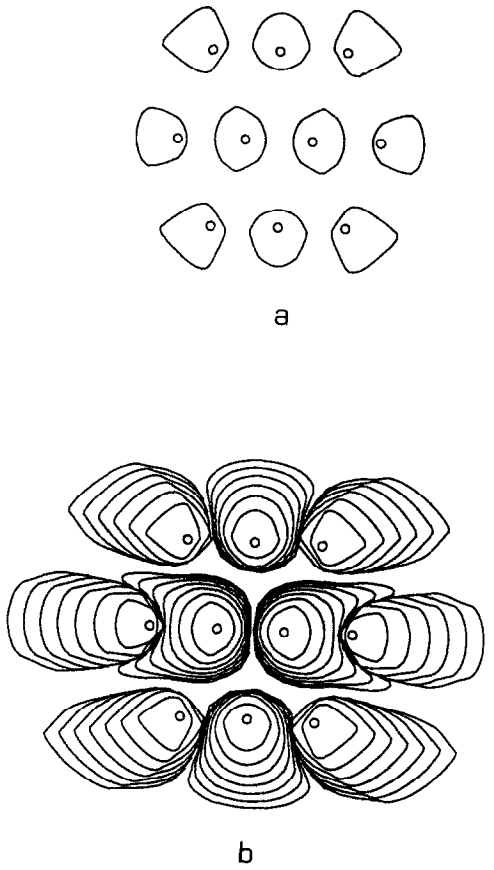

Fig. 3. Time-varying solute front positions corresponding to the reference flow field. The flow field, simulated using parameter values from Dillaman (1984), roughly corresponds to that in chick femurs. The canals' angle of inclination (ϕ_0) and non-dimensional radii (R) are 10° and 0.01, respectively, while the non-dimensional source strength (m) and non-dimensional cross-cortical velocity (Γ_0) are both equal to $6(10^{-6})$. Note that R is the ratio of canal radius to cortex thickness while Γ_0 is the ratio of the cross-cortical velocity to the cross-cortical velocity scale. In addition, m is equal to the outward velocity at the canal wall, $\overline{V^*}$, divided by the cross-cortical velocity scale, $\overline{\Gamma^*}$, and multiplied by R. In (a), the non-dimensional time, t, ($= t^*/(T^*/\overline{\Gamma^*})$) equals 100. In (b), the dimensionless time increment ($\Delta t = \Delta t^*/(T^*/\overline{\Gamma^*})$) between succeeding fronts is 20. Note, the periosteal and endosteal surfaces are located to the left and right of each plot, respectively.

with solute being pushed toward the periosteal surface, at larger values of Γ_0 (Fig. 7(b)–(d)). At the highest cross-cortical velocities, solute haloes appear to maintain their initial size and shape while traveling toward the periosteal surface (Fig. 7(d)).

Although not shown, it is found that solute coverage is independent of the source strength m. However, the time required for all solute particles to pass out of the solution domain decreases with increasing m.

DISCUSSION

The study's first objective was to develop a simple model of circulatory interstitial flow and transport within porous cortical bone, taking into account vessel canal outflow, canal inclination and shape, and cross-cortical flow. The second objective was to validate the model by comparing predicted transport characteristics with experimental observations. Finally, the model was to be used to investigate the effects of canal radius, canal inclination, and cross-cortical velocity on interstitial solute transport.

Prior to discussing the results, we consider the validity of various assumptions underlying the model. Since canal radii typically fall within a fairly narrow range of values (Pollack *et al.*, 1984) and since cross-cortical canals are typically close to parallel (see, e.g. Dillaman, 1984), the assumptions (1 and 3) that all canals are mutually parallel and of equal radius appear to be reasonable in the present first-order model. Replacing an angular cross-section of the cortex with a rectangular section (assumption 4) is reasonable if: (i) the ratio of azimuthal intercanal spacing (i.e. the average azimuthal distance between canals) to the bone's circumference is small and, (ii) relatively few canals are included in the solution domain (so that the azimuthal length of the domain is small compared to the bone's circumference). Since the ratio of azimuthal intercanal spacing to bone circumference is of the order of 0.01 in both chick cortical bone (Dillaman, 1984) and canine bone (Rhinelander, 1972) and since the solution domain is limited to three rows of canals, this also appears to be a reasonable simplification. The assumption that the mineralized matrix is homogeneous and continuous (assumption 6) represents an idealization since the matrix contains numerous osteocytic lacunae and associated canalicular networks. (Note, lacunae are small ellipsoidal cavities enclosing single bone cells, or osteocytes; canaliculi are microscopic channels that pass out of lacunae, connecting a given lacuna to neighboring lacunae and to a parent vessel canal. In Fig. 1, osteocytic lacunae appear as small ferritin-filled cavities surrounding each vessel canal.) However, if the characteristic lacunar length L_ℓ^* (e.g. major axis length) is much smaller than the smallest characteristic length in the idealized problem (i.e. the canal radius R^*), then the matrix can be taken as continuous. Based on Dillaman's (1984) photomicrographs and on data given by Pollack *et al.* (1984), the ratio of L_ℓ^* to R^* ranges from 0.1 to 0.2, suggesting the validity of a continuum approach. Note that Petrov *et al.* (1989), using a continuum assumption, accurately predicted stress-induced streaming potentials within osteons. With regard to assumption (9), although circulatory flow is not perfectly periodic, the assumption of perfect periodicity is a reasonable first approximation. The assumption that canal outflow can be modeled as line source flow (assumption 12) is suggested by the patterns of marker movement near vessel canals and is

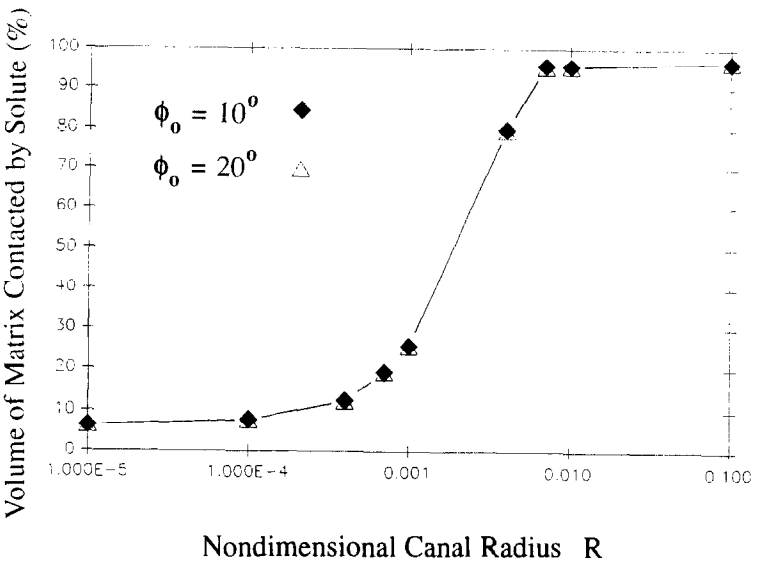

Fig. 4. Fraction of matrix within the solution domain contacted by solute (expressed as a percentage), given as a function of the dimensionless canal radius R and angle of inclination ϕ_0. The amount of solute contact with the surrounding matrix increases with increasing R. The range of R over which solute coverage increases to high levels ($0.001 \leqslant R \leqslant 0.01$) roughly corresponds to the range of R values observed in humans and chicks. Over the range of R's shown, solute coverage is essentially independent of the canals' angle of inclination. In all cases, $m = \Gamma_0 = 6(10^{-6})$. Refer to the caption to Fig. 3 for definitions of the non-dimensional parameters.

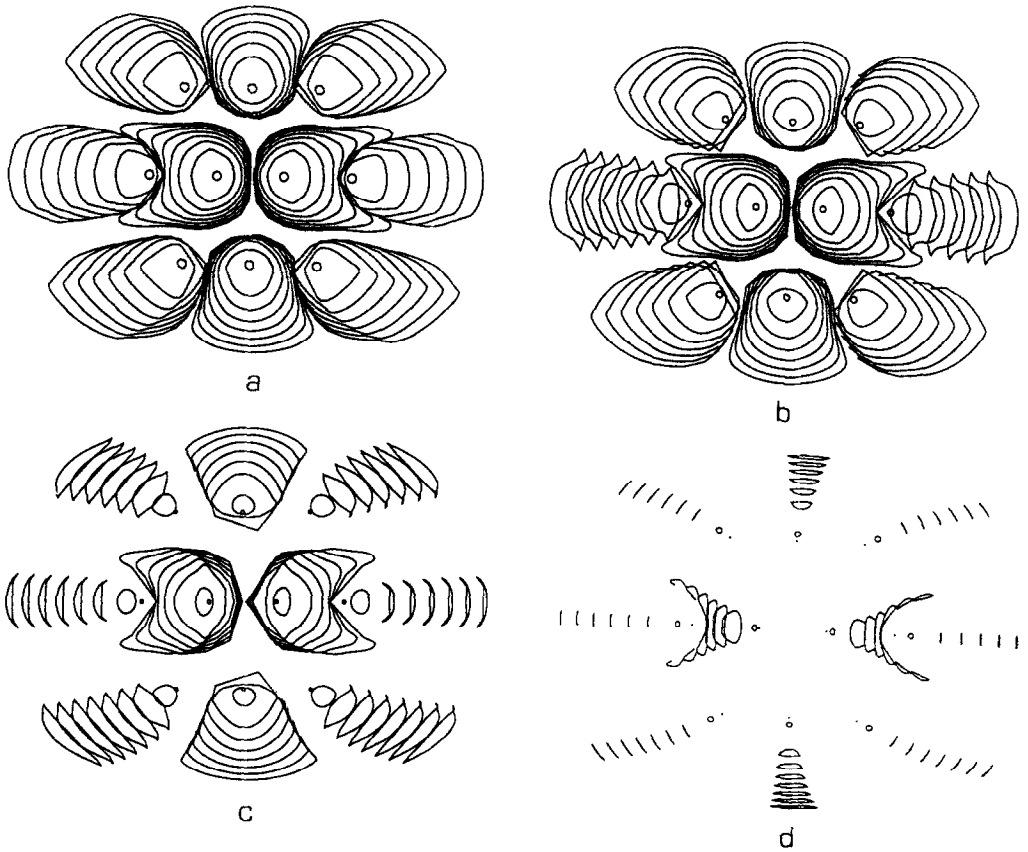

Fig. 5. Time-varying solute front positions as a function of the dimensionless canal radius R: (a) $R = 0.01$, (b) $R = 0.007$, (c) $R = 0.004$, (d) $R = 0.001$. This shows that lateral solute spread and consequent solute-matrix contact decreases significantly over a single decade in $R(0.001 \leqslant R \leqslant 0.01)$. Solute contact is greater than 95% for $R \geqslant \sim 0.01$ and less than 10% for $R \leqslant \sim 0.0001$ (refer to Fig. 4). The endosteal and periosteal surfaces are located to the left and right of each plot, respectively. Note the slight asymmetry in solute propagation as solute is pushed from the endosteal surface toward the periosteal surface. In all cases, $\phi_0 = 10°$, $m = \Gamma_0 = 6(10^{-6})$. Refer to the caption to Fig. 3 for definitions of the non-dimensional parameters. The dimensionless time increment between succeeding fronts is 20.

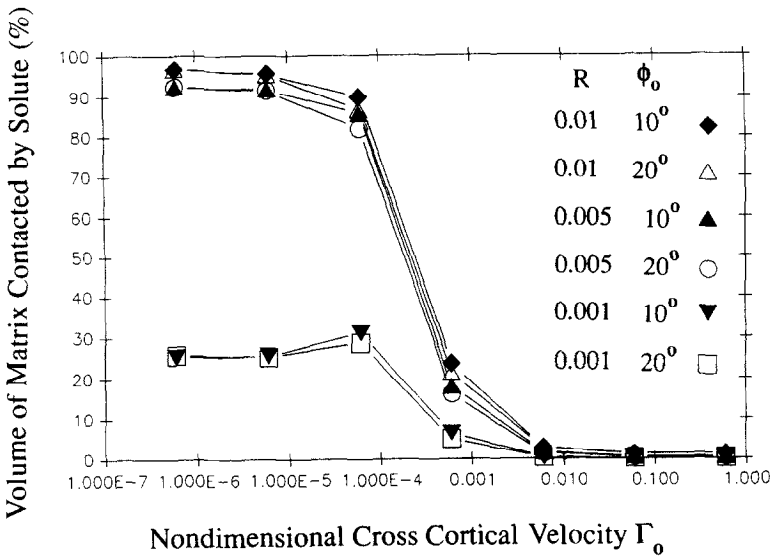

Fig. 6. Fraction of matrix within the solution domain contacted by solute (expressed as a percentage), given as a function of the non-dimensional cross-cortical velocity (Γ_0), the non-dimensional canal radius (R), and the canals' angle of inclination (ϕ_0). For each value of R, the level of solute coverage is highest for $\Gamma_0 \leq \sim 0.0001$. In contrast, coverage approaches zero as Γ_0 approaches 1. For each R, solute coverage is essentially independent of the angle of inclination ϕ_0. In all cases, the canal source strength, m, equals $6(10^{-6})$. Refer to the caption to Fig. 3 for definitions of the non-dimensional parameters.

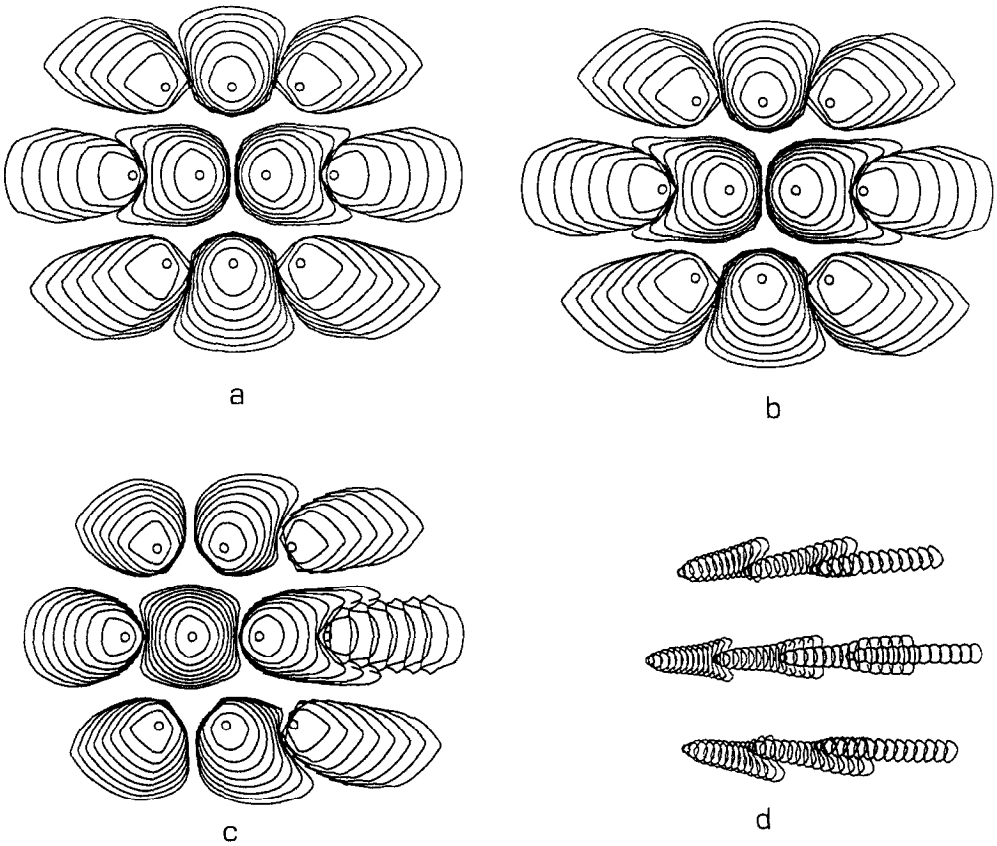

Fig. 7. Time-varying solute front positions as a function of dimensionless cross-cortical velocity Γ_0. Solute coverage decreases with increasing cross-cortical velocity since the ratio of lateral to cross-cortical displacement during any time increment decreases with increasing Γ_0. Thus, particles are confined to smaller lateral regions at larger values of Γ_0. Asymmetry in solute coverage clearly increases with increasing cross-cortical velocity. Note that the endosteal and periosteal surfaces are located to the left and right of each plot, respectively. In all cases, $R = 0.01$, $\phi_0 = 10°$, and $m = 6(10^{-6})$. The dimensionless time increment between succeeding fronts is 20: (a) $\Gamma_0 = 0$, (b) $\Gamma_0 = 6(10^{-6})$, (c) $\Gamma_0 = 6(10^{-4})$, (d) $\Gamma_0 = 6(10^{-3})$ Refer to the caption to Fig. 3 for definitions of the non-dimensional parameters.

valid when the ratio of canal radius (R^*) to the characteristic distance (H^*) between canals is small (Keanini, 1994). When this condition holds, outflow from canals appears as line source flow at distances on the order of H^*. Since the ratio of R^* to H^* is of the order of 0.1 in chick femurs (Dillaman, 1984), approximately 0.05 to 0.2 in canine long bones (Rhinelander, 1972), and approximately 0.05 to 0.3 in human long bones (Pidaparti and Burr, 1992), this again appears to be a reasonable approximation. (Note, H^* could be taken as either d_4^* or d_2^* in Fig. 2(b) since both distances are of the same order of magnitude.) Finally, the assumption (12) that all canals have equal strengths can be relaxed to allow differing ms (or equivalently, different outflow velocities and/or differing canal radii). However, this level of specialization is deemed unnecessary in a first-order model and, moreover, would be difficult to implement using present marker data.

Predicted solute transport characteristics for the reference case (Fig. 3) are qualitatively consistent with Dillaman's (1984) observations (Fig. 1). Although not shown, model predictions are also consistent with the observations reported by Montgomery *et al.* (1988). The model thus suggests that the semi-elliptical halo shapes observed by Dillaman (1984) and Montgomery *et al.* (1988) reflect: (i) superposition of pressure fields induced by several neighboring canals and, (ii) projection of semi-circular haloes (on planes z = constant) onto the plane of cross-section (where the haloes appear elliptical). The model also captures the displacement of solute toward the periosteal surface, as observed by Dillaman (1984) and Montgomery *et al.* (1988) (Figs 5 and 7). Thus, the model supports the view that the displacement is caused by cross-cortical interstitial flow (Dillaman, 1984; Montgomery *et al.*, 1988). Assuming that the displacement indeed reflects cross-cortical flow, and noting that the largest matrix pores (~ 100 nm characteristic diameter) in porous cortical bone are only an order of magnitude smaller than the average diameter of canaliculi (McCarthy and Yang, 1992), then the results of Dillaman (1984) and Montgomery *et al.* (1988) suggest that circulatory interstitial cross-cortical flow, originating at the endosteum, could represent a significant osteocytic nutrient supply route.

The finding that solute coverage is sensitive to canal radius (Figs 4 and 5) appears to be a new result. Importantly, the model indicates that coverage increases from relatively low levels to high levels over a range of Rs ($\sim 0.001 < R < \sim 0.01$) that essentially coincides with the range of Rs found in humans ($\sim 0.003 < R < \sim 0.006$; Mihalko *et al.*, 1992; Pollack *et al.*, 1989) and chicks ($\sim 0.005 < R < \sim 0.01$; Dillaman, 1984). This suggests that within porous cortical bone, the ratio of canal radius to cortex thickness (R) promotes near-optimal species contact with the matrix. This view is supported by the fact that coverage is maximized near physiologically realistic R values (i.e. near $R > \sim 0.01$; see Fig. 5). Although simulations show that complete coverage occurs at R values larger than 0.1, actual R values appear to rarely achieve magnitudes this large. This may reflect the fact that the cross-sectional area of mineralized bone, and thus the bone's load-carrying capacity, decreases with increasing R. Observed R values may thus be the *minimum* values that allow complete or near-complete specie-matrix contact; larger R values may reduce structural strength to insufficient levels.

The model suggests that species-matrix contact (within porous cortical bone) may be enhanced during periods of intra-canal resorption and suppressed during periods of intra-canal deposition (resulting in canal enlargement and shrinkage, respectively). Since extended periods of reduced loading can induce resorption (see, e.g. Dillaman *et al.*, 1991), and since stress-induced interstitial flow likely predominates over circulatory interstitial flow (at least under most external load conditions; see Piekarski and Munro, 1977), then the model suggests that reduced-load-induced resorption may effectively compensate for reduced or non-existent stress-induced flow by enhancing circulatory flow and species transport. Experimental evidence is needed in order to fully address this intriguing question, however.

Solute coverage is maximized only when the cross-cortical velocity (Γ_0) is less than or equal to (approximately) $6(10^{-5})$ (Fig. 6). Since $m/\Gamma_0 = \overline{V^*}R/\overline{\Gamma_0^*}$, and since $m = 6(10^{-6})$ in these calculations, then it is seen that coverage is maximized when the ratio of actual velocities $\overline{V^*}/\overline{\Gamma_0^*}$ is greater than $\sim 0.1/R$. Thus, for the range of Rs shown, maximum coverage occurs when the canal outflow velocity ($\overline{V^*}$) is, at minimum, one ($R = 0.01$) to two ($R = 0.001$) orders of magnitude larger than the cross-cortical velocity ($\overline{\Gamma_0^*}$). Physically, optimal coverage requires that the canal outflow velocity be of sufficient magnitude relative to the cross-cortical velocity to allow significant lateral solute propagation (in xy-planes) into the matrix. In contrast, when the cross-cortical velocity is high relative to $\overline{V^*}$, lateral displacements are small as solute particles are rapidly swept across the cortex (Fig. 7). These results suggest that the relatively impermeable appositional layers of bone that often underlie the periosteal surface (Montgomery *et al.*, 1988) may enhance species coverage by limiting cross-cortical flow. If we surmise that nature has optimized cross-cortical flow to allow maximum species contact with cells within the matrix, then the actual cross-cortical velocity ($\overline{\Gamma_0^*}$) will be less than approximately 0.0001 $\overline{\Gamma^*}$ (see Fig. 6; note $\overline{\Gamma^*} = k(\overline{P_c^*} - \overline{P_p^*})/(T^*\mu)$). Again, however, experimental data are needed in order to address this question.

In summary, parametric studies based on the present theoretical model lead to four principal findings: (1) Model transport characteristics are qualitatively consistent with the experimental observations reported by Dillaman (1984) and Montgomery *et al.* (1988). (2) Solute contact with the matrix is maximized

when the ratio of canal radius to cortex thickness, R, is near physiological R values. (3) Solute–matrix contact decreases to relatively low levels when R falls below the physiological range. (4) Solute–matrix contact is maximized when the cross-cortical velocity is approximately an order of magnitude smaller than the canal outflow velocity. The first three findings suggest that within porous bone physiological ranges of R promote near-optimal species contact with the mineralized matrix. The fourth finding suggests that relatively impermeable layers of bone within the cortex can effectively promote solute-matrix contact by limiting cross-cortical flow. Finally, the model suggests that intra-canal resorption associated with reduced external loading may effectively compensate for reduced, stress-induced interstitial flow by enhancing circulatory interstitial flow and species transport.

Acknowledgement—All calculations were carried out at North Carolina Supercomputing Center.

REFERENCES

Brooks, M. (1971) *The Blood Supply of Bone.* Butterworths, Ltd., London.

Dillaman, R. M. (1984) Movement of ferritin in 2-day-old chick femur. *Anat. Rec.* **209,** 445–453.

Dillaman, R. M., Roer, R. D. and Gay, D. M. (1991) Fluid movement in bone: theoretical and empirical. *J. Biomechanics* **24,** 163–177.

Doty, S. B., Robinson, R. A. and Schofield, B. H. (1976) Morphology of bone and histochemical staining characteristics of bone cells. *Handbook of Physiology,* Vol. 7 (Edited by Greep, R. O. and Atwood, E. B.), pp. 3–23. American Physiological Society, Washington.

Fox, R. W. and McDonald, A. T. (1992) *Introduction to Fluid Mechanics.* Wiley, New York.

Johnson, M. W., Chakkalakal, D. A., Harper, R. A. and Katz, J. L. (1982) Fluid flow in bone *in vitro*. *J. Biomechanics* **15,** 881–885.

Jowsey, J. and Gordan, G. (1971) Bone turnover and osteoporosis. In *The Biochemistry and Physiology of Bone,* Vol. 3. Academic Press, New York.

Keanini, R. (1994) The effect of anisotropic permeability on fluid flow in bone. *Proc. 16th Ann. Int. Conf. on IEEE EMBS* (to appear).

Kufahl, R. H. and Saha, S. (1990) A theoretical model for stress-generated fluid flow in the canaliculi-lacunae network in bone tissue. *J. Biomechanics* **23,** 171–180.

McCarthy, I. D. and Yang, L. (1992) A distributed model of exchange processes within the osteon. *J. Biomechanics* **25,** 441–450.

Mihalko, W. M., Beaudoin, A. J., Cardea, J. A. and Krause, W. R. (1992) Finite-element modeling of femoral shaft fixation techniques post total hip arthroplasty. *J. Biomechanics* **24,** 127–136.

Montgomery, R. J., Sutker, B. D., Bronk, J. T., Smith, S. R. and Kelly, P. J. (1988) Interstitial fluid flow in cortical bone. *Microvasc. Res.* **35,** 295–307.

Otter, M. W., Palmieri, V. R. and Cochran, G. V. B. (1990) Transcortical streaming potentials are generated by circulatory pressure gradients in living canine tibia. *J. orthop. Res.* **8,** 119–126.

Petrov, N., Pollack, S. and Blagoeva, R. (1989) A discrete model for streaming potentials in a single osteon. *J. Biomechanics* **22,** 517–521.

Pidaparti, R. M. and Burr, D. B. (1992) Collagen fiber orientation and geometry effects on the mechanical properties of secondary osteons. *J. Biomechanics* **25,** 869–880.

Piekarski, K. and Munro, M. (1977) Transport mechanism operating between blood supply and osteocytes in long bones. *Nature* **269,** 80–82.

Pollack, S. R., Petrov, N., Salzstein, R., Brankov, G. and Blagoeva, R. (1984) An anatomical model for streaming potentials in osteons. *J. Biomechanics* **17,** 627–636.

Rhinelander, F. W. (1972) Circulation in bone. In *The Biochemistry and Physiology of Bone,* Vol. 2. Academic Press, New York.

Roer, R. D., Dillaman, R. M. and Rutherford, E. (1988) Molecular marker distribution and computer modeling of rat bone fluid dynamics. *J. Bone Miner. Res.* **3,** S186.

Seliger, W. G. (1970) Tissue fluid movement in compact bone. *Anat. Rec.* **166,** 247–256.

Willans, S. M. and McCarthy, I. D. (1986) Distributed model of blood-bone exchange. *J. biomed. Engng.* **8,** 235–243.

Zienkiewicz, O. C. (1977) *The Finite Element Method* (3rd Edn). McGraw-Hill, Maidenhead.

APPENDIX A

In order to relate L^* to L_0^*, we extend the dashed lines at $Z^* = 0$ and $Z^* = L^*$ into the top left and bottom right corners (respectively) of the bounding solid rectangle CGED (shown in Fig. A1, which is taken from Fig. 2(c)). We then form the right triangles ΔADE, ΔABC and ΔCFG. First note that

$$L_0^* = \overline{DA} + \overline{AC}. \tag{A1}$$

Referring to ΔADE and ΔABC, it is seen that

$$\overline{DA} = T^* \tan\phi_0 \text{ and } \overline{AC} = L^*/\cos\phi_0. \tag{A2}$$

Using equation (A2) in equation (A1) and rearranging we obtain a relationship between L^* and L_0^*:

$$L^* = (L_0^* - T^* \tan\phi_0)\cos\phi_0. \tag{A3}$$

L_0^* can be related to the cortex thickness T^* and to the height X_0^* of the solution domain as follows. First note that

$$\overline{BC} = \overline{FBC} - X_0^* = T^*/\cos\phi_0 - X_0^*, \tag{A4}$$

where we have inserted the length of the line segment FBC in the right equality ($\overline{FBC} = T^*/\cos\phi_0$). Referring to ΔABC, we see that $\overline{BC}$ is also given by

$$\overline{BC} = \overline{AC}\sin\phi_0. \tag{A5}$$

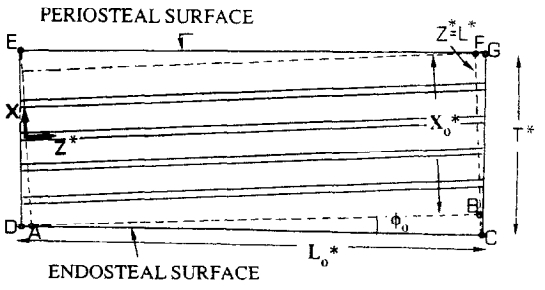

Fig. A1. Lateral view of the solution domain (adapted from Fig. 2(c)). The right triangles ΔADE, ΔABC and ΔCFG are formed by extending the dotted line segments at $Z^* = 0$ and $Z^* = L^*$ into the upper left and lower right corners of the solid rectangle CGED. Note that angles ∠EDA, ∠ABC and ∠FGC are right angles and that angles ∠DEA, ∠BAC and ∠FCG all equal ϕ_0.

Replacing $\overline{AC}$ with the second relationship in (A2) and then substituting the right-hand side of (A3) for L^* we obtain

$$\overline{BC} = (L_0^* - T^* \tan \phi_0)\sin \phi_0. \tag{A6}$$

Finally, equating the right-hand sides of (A4) and (A6) and solving for L_0^* we obtain a relationship between L_0^* and T^* and X_0^*:

$$L_0^* = T^*(1 + \sin^2\phi_0)/(\cos \phi_0 \sin \phi_0) - X_0^*/\sin \phi_0. \tag{A7}$$